ACS APPLIED MATERIALS & INTERFACES

Research Article

www.acsami.org

Surfactant Assistance in Improvement of Photocatalytic Hydrogen Production with the Porphyrin Noncovalently Functionalized Graphene Nanocomposite

Mingshan Zhu,[§,‡] Zhi Li,[§,†] Bin Xiao,[†] Yongtao Lu,[†] Yukou Du,[†] Ping Yang,*[,†] and Xiaomei Wang[†]

[†]College of Chemistry, Chemical Engineering and Materials Science, Soochow University, Suzhou, 215123, China

[‡]CAS Key Laboratory of Colloid, Interface and Chemical Thermodynamics, Institute of Chemistry, Chinese Academy of Sciences, Beijing, 100190, China

Supporting Information

ABSTRACT: In this paper, a 5,10,15,20-tetrakis(4-(hydroxyl)-phenyl) porphyrin (TPPH) noncovalently functionalized reduced graphene oxide (RGO) nanohybrid has been facilely synthesized by immobilizing TPPH on RGO nanosheets. This nanohybrid was characterized by atomic force microscopy (AFM), transmission electron microscopy (TEM), and UV−vis spectra, which demonstrated that the TPPH molecule was attached on the surface of the graphene nanosheet. The results of fluorescence quenching and photocurrent enhancement of TPPH−RGO exhibit that the fast electrons transfer from photoexcited TPPH molecules to RGO sheets. Compared with bare TPPH or RGO functional Pt nanoparticles, the TPPH-sensitized RGO loaded with Pt nanoparticles shows remarkable enhanced photocatalytic activity under UV−vis light irradiation. The superior electron-accepting and electron-transporting properties of graphene greatly accelerate the electron transfer from excited TPPH to Pt catalysts, which promote the photocatalytic activity for hydrogen evolution. More importantly, with the assistance of cetyltrimethylammonium bromide (CTAB) surfactant, the catalytic activity and stability is further improved owing to aggregation prevention of TPPH−RGO nanocomposites. Our investigation might not only initiate new opportunities for the development of a facile synthesis yet highly efficient photoinduced hydrogen evolution system (composed of organic dye functionalized graphene) but also pave a new avenue for constructing graphene-based matericals with enhanced catalytic performance and stability under surfactant assistance.

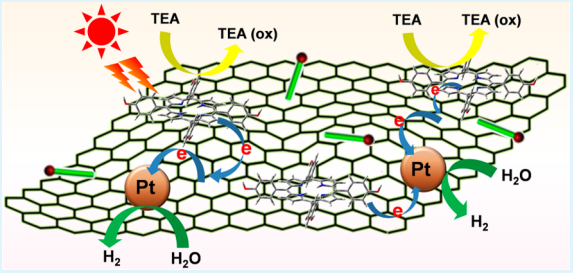

KEYWORDS: *noncovalently functionalized graphene, porphyrin, electron transfer, photocatalysis, hydrogen evolution, surfactant*

1. INTRODUCTION

Hydrogen, as a zero carbon emission fuel, is forecast to become a major source of energy in the future.[1−3] Among the wide variety of hydrogen generation tactics, hydrogen production from light-induced water splitting in the presence of a photocatalyst has attracted enormous attention because it is cost effective and ecofriendly. Since Fujishima and Honda[4] first reported the photoelectrochemical splitting of water into H_2 and O_2 on a TiO_2 semiconductor electrode, a large amount of photocatalytic systems for light-driven hydrogen evolution have been developed.[5−16] Among them, dye-sensitized photocatalysts, however, have received remarkable increasing attention because their optical and chemical properties can be understood and strategically tuned on the molecular level.[11−16] On the other hand, porphyrin-based complexes as light-harvesting materials play an important role in photosynthesis. Due to their large π-conjugated aromatic system and outstanding chemical and thermal stability, porphyrin-based materials have been widely used as photosensitizers in the fields of optical device, dye-sensitized fuel cell, and photocatalytic hydrogen evolution.[14−19]

On another front, graphene, a single layer of sp^2-bound carbon atoms extended to form a two-dimensional nanostructure, has been regarded as a new generation of solar energy materials.[20−25] Since it possesses excellent optical transmittance, large specific surface area, and a conspicuous locally conjugated aromatic network, graphene is valuable in promoting charge separation, which makes it an ideal candidate as a photocatalyst carrier or promoter. To date, graphene (e.g., graphene oxide, viz., GO, and reduced graphene oxide, viz., RGO) based photocatalysts have become one of the hottest topics in the photocatalytic area.[22−24] The graphene-based photocatalysts prepared by immobilizing inorganic semiconductors[26−38] or organic dye sensitizers[39−43] on graphene sheets have demonstrated very nice catalytic activity for photoinducing water reduction to produce hydrogen. Among these photocatalysts, the chemical functionalization of graphene with a dye offers a practical strategy to combine the unique properties of each component and a potential to control the

Received: November 30, 2012
Accepted: February 5, 2013
Published: February 5, 2013

conjugate photoelectric properties such as light absorption, efficiency of charge transport and separation, and photocatalytic performances.[44,45] In general, organic molecule functionalized graphene can be prepared by either covalent or noncovalent interaction. However, covalently functionalized graphene, owing to its complicated synthesis and low yield, is limited to its extensive application. On the contrary, these noncovalently modified graphenes are mainly through molecular interactions, such as electrostatic interaction, $\pi-\pi$ stacking, or hydrogen bonding between graphene and organic molecules, which received remarkable increasing attention since the synthesis is facile.[44,45]

As known, the graphene can not be well dispersed in aqueous solution since it is a hydrophobic substance and can easily aggregate by strong $\pi-\pi$ interactions, which might decrease the photocatalytic performance and stability. On the other hand, many surfactants could easily interact with graphene by ionic interactions or $\pi-\pi$ interactions to enhance the distribution of graphene in various solvents without aggregation.[46−48] This merit might endow surfactant-assistant graphene-based photocatalysts with enhanced catalytic activity and stability by improving solubility and aggregation prevention. Thus, to develop surfactant-assistant efficient dye-functionalized graphene-based photocatalysts for hydrogen evolution is a significant subject.

In this paper, we report the preparation, characterization, and photocatalysis of a 5,10,15,20-tetrakis(4-(hydroxyl)phenyl) porphyrin (TPPH) noncovalently functionalized reduced graphene oxide nanocomposite (TPPH−RGO). Choosing TPPH as a sensitizer to hybridize with graphene is not only due to that TPPH can easily hybridize with graphene through strong $\pi-\pi$ stacking interactions but also due to its nice locally conjugated aromatic structure, as well as its remarkable chemical and thermal stability benefitting for photocatalytic reactions.[17−19] The fluorescence quenching and photocurrent experiments of TPPH−RGO display that the photoexcited electrons could transfer efficiently from TPPH molecules to RGO nanosheets. Furthermore, efficient and stable light-driven photocatalytic hydrogen evolution was observed from Pt nanoparticle modified TPPH−RGO (TPPH−RGO/Pt). Compared with TPPH-functionalized Pt colloid or Pt-modified RGO, the TPPH−RGO/Pt nanocomposite exhibited remarkable enhanced photocatalytic activity, which was attributed to the superior electron-accepting and electron-transporting abilities of graphene. More importantly, with the assistance of cetyltrimethylammonium bromide (CTAB), the catalytic activity and stability is further improved owing to aggregation prevention of the TPPH−RGO/Pt nanocomposite. The photocatalytic activity of TPPH−RGO/Pt is systematically investigated by comparing different parameters such as pH value and the composition of the nanocomposite. As far as we know, this work might be the first report concerning a surfactant-enhanced porphyrin noncovalently functionalized graphene for photocatalytic hydrogen evolution. This investigation might open up new possibilities for the development of stable photocatalysts via organic photosensitizers functionalizing graphene with the assistance of surfactants for solar energy conversion.

2. MATERIALS AND METHODS

2.1. Materials. 5,10,15,20-Tetrakis(4-(hydroxyl)phenyl) porphyrin (TPPH, Sigma-Aldrich, 95%), dihydrogen hexachloroplatinate (IV) hexahydrate (H_2PtCl_6, Alfa Aesar, >99.9%), cetyltrimethylammonium bromide (CTAB, Aifa Aesar, 95%), and graphite powder (Alfa Aesar, 325 mesh, 99.9995%) were used as received without further treatments. All of the other chemicals (analytical reagent grade) were purchased from Sinopharm Chemical Reagent Company and used without further purification.

2.2. Synthesis of Graphene Oxide (GO) and RGO Nanosheets and Platinum Nanoparticle Modified RGO Nanosheets. GO nanosheets were synthesized through the chemical exfoliation of graphite powder by using a modified Hummers' method.[25] The detailed synthesis procedure was carried out according to the methods described previously.[25]

RGO was obtained by a chemical reduction of GO under alkaline conditions according to the procedures reported.[39,42,43] First, 3 μL of hydrazine solution (85%) was added to 20 mL of GO (1 mg mL^{-1}) aqueous colloidal suspension, and the pH value of the mixture was adjusted to 10 with potassium hydroxide aqueous solution (1 M). The mixture was heated to 90 °C and kept at the temperature for 2 h. The yellow-brown suspension turned into black after the reduction reaction (Figure S1, Supporting Information). The bulk precipitate was removed by low-speed centrifugation (800 rpm, 5 min) and subsequent filtration through a Nylon film yielded black solids, which were washed with distilled water five times. Finally, the wet solids were redispersed into water by ultrasonic treatment, resulting in RGO aqueous suspension (0.2 mg mL^{-1}).

Platinum nanoparticle modified RGO nanosheets (RGO/Pt) were prepared using an ethanol reduction method.[13,14] In a typical experiment, 1 mL of aqueous solution of H_2PtCl_6 (7.723 mmol L^{-1}) was added to 20 mL of RGO (0.1 mg mL^{-1}) aqueous ethanol (V_{water}:$V_{ethanol}$ = 1) suspension, and the mixture was adjusted to a pH value of 10 by addition of NaOH aqueous solution. The mixture was heated under reflex for 2 h, resulting in a dark brown RGO/Pt nanocomposite. On the other hand, TPPH-sensitized Pt colloid solution (TPPH/Pt) was also prepared using the same method for the purpose of comparison.

2.3. Preparation of TPPH−RGO Hybrids and TPPH−RGO/Pt Nanocomposites. TPPH ethanol solution (0.5 mg mL^{-1}) was mixed with RGO suspension (0.1 mg mL^{-1}) in a 50 mL flask at different ratios (the volume of ethanol used is controlled below 5 vol % of the total volume of RGO solution). The mixture was bath-sonicated for 30 min and then stirred at room temperature for 12 h, resulting in TPPH−RGO hybrids. Using RGO/Pt instead of RGO suspension, the TPPH−RGO/Pt nanocomposite was prepared using the same method.

2.4. Photocatalytic Performances. The photocatalytic reaction was carried out in a 70 mL quartz flask equipped with a flat optical entry window. In a typical photocatalytic experiment, 50 mL of aqueous solution of triethanolamine (TEA, 10 vol %) containing 5 mL of TPPH−RGO/Pt solution (ca. 1 mg) and 2 mg of cetyltrimethylammonium bromide (CTAB) were added into the quartz flask. The pH value of the solution was adjusted to 9 by addition of hydrochloric acid. Prior to irradiation, the mixture was sonicated for 30 min to form a homogeneous suspension. The system was deaerated by bubbling argon into the solution for 30 min before light irradiated. The solution was stirred continuously and irradiated by a GY−10 xenon lamp (150 W) at 298 K. The distance between the flask and the lamp was maintained at 15 cm. The gas production was measured using an online gas chromatograph (GC1650) equipped with a thermal conductivity detector (TCD), where Ar was used as a carrier gas. The standard H_2/Ar gas mixtures of known concentrations were used for GC signal calibration. The yield of hydrogen is defined as the moles of H_2 (n) evolved over per gram of used catalyst (m) in a certain reaction time (t).

$$\text{yield } (H_2) = \frac{n_{H_2}}{m_{\text{catalyst}}} \quad (1)$$

The quantum yields of hydrogen (Φ_{H2}) are defined by the following equation

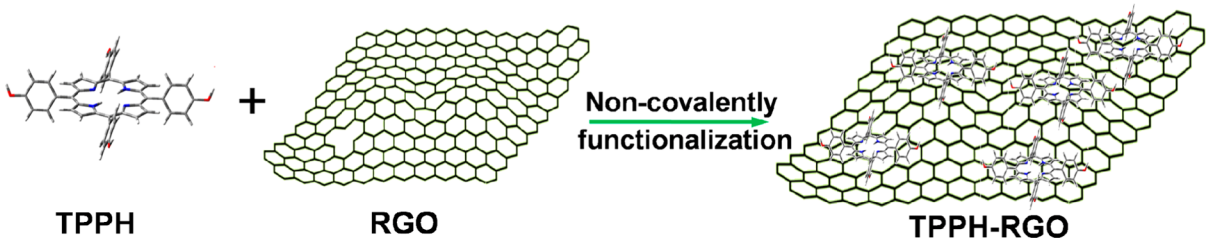

Figure 1. Illustration of formation of the TPPH−RGO nanocomposite via noncovalent functionalization.

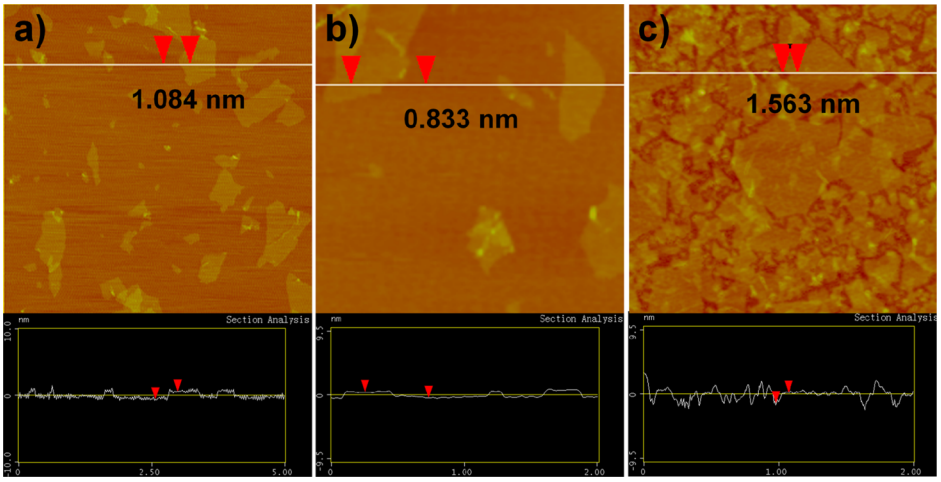

Figure 2. AFM images of GO (a), RGO (b), and TPPH−RGO (c) nanosheets.

$$\Phi_{H_2} = \frac{n_{H_2} \times 2}{I_0 \times t} \times 100\% \quad (2)$$

where I_0 was the number of incident photons per second. I_0 was found to be 7.22×10^{-9} mol s^{-1}.

2.5. Apparatus and Measurements. Atomic force microscopy (AFM) images were recorded on a Digital Instrument Nanoscope IIIa Multimode system (Santa Barbara, CA) with a silicon cantilever by using the tapping mode. The diluted colloidal dispersion (0.01 mg mL^{-1}) was sprayed onto a freshly cleaved mica surface and dried in air at room temperature. Transmission electron microscopy (TEM) studies were conducted on a TECNAI−G20 electron microscope operating at an accelerating voltage of 200 kV. X-ray diffraction (XRD) patterns of the samples were obtained with a Philips diffractometer using Ni-filtered Cu Kα radiation. UV−vis absorption spectra of the samples were recorded on a TU1810 SPC spectrophotometer. Fluorescence spectra were recorded using a FL-2500 fluorospectrophotometer. Raman spectra were measured with a Jobin Yvon HR-800 spectrometer using a He−Ne laser (λ = 633 nm, spot size ~ 1 μm). Fourier transform infrared (FT-IR) spectra were obtained with a Thermo Scientific Nicolet 6700 instrument. X-ray photoelectron spectroscopy (XPS) measurements were taken by an AXIS Ultra DLD system (Kratos Analytical Inc.) using monochromatic Al Kα radiation. The samples for XPS measurements were prepared by dropping the dilute colloidal dispersion onto a silicon wafer and dried in air at room temperature. Binding energies were calculated with respect to C (1s) at 284.6 eV. The measurement of photoelectrical response was performed with a CHI660B potentiostat/galvanostat electrochemical analyzer in a three-electrode system consisting of an indium tin oxide (ITO) covered with sample, a platinum wire, and a saturated calomel electrode (SCE). The ITO covered with sample acted as a working electrode, the platinum wire as the counter electrode, and the SCE as the reference electrode. The surface of the working electrode exposed to the electrolyte was a square film with the surface areas of 0.8 cm^2 .The supporting electrolyte was TEA mixed with 0.1 M Na_2SO_4 aqueous. The working electrode was irradiated with a GY-10 xenon lamp (150 W) during the measurement.

3. RESULTS AND DISCUSSION

3.1. Preparation and Morphology Characteristics of the TPPH−RGO Hybrid Nanocomposite. Experimentally, TPPH ethanol solution (0.5 mg mL^{-1}) was mixed with RGO suspension (0.05 mg mL^{-1}) in a 50 mL flask at different volume ratio. The mixture was bath-sonicated for 30 min and then stirred for 12 h at room temperature, resulting in a TPPH−RGO nanohybrid. Figure 1 shows the preparation process of TPPH−RGO. In general, this noncovalent modification of graphene is mainly through intermolecular interactions between graphene and the organic molecule, such as electrostatic interaction, $\pi-\pi$ stacking interaction, etc.[44,45] Owing to the negative charged RGO in aqueous solution, TPPH could not easily assemble on RGO by electrostatic interaction. As it is well-known that porphyrin molecules, which have a two-dimensional 18-π-electron aromatic structure, could interact with graphene through $\pi-\pi$ stacking, they thus facilitate the formation of the TPPH−RGO hybrid nanocomposite. The great advantages of the strategy of noncovalent functionalization graphene are that it can combine the unique properties of the chromophore and graphene, while it does not disturb the physical properties of both moieties.[44,45]

The surface morphology and height profile of the samples were observed by AFM. As shown in Figure 2, we can observe individual GO sheets clearly with 200−1000 nm lateral width. The AFM images show that the average thicknesses of monolayer GO and RGO were around 1.084 nm (Figure 2a) and 0.833 nm (Figure 2b), respectively. The thickness of RGO is lower than that of GO, owing to the elimination or diminishment of oxygen-containing functional groups (−OH, −COOH, C−O−C) on the sheet surfaces, suggesting that GO was successfully reduced. Interestingly, compared with RGO, the average thickness of the TPPH−RGO nanocomposite

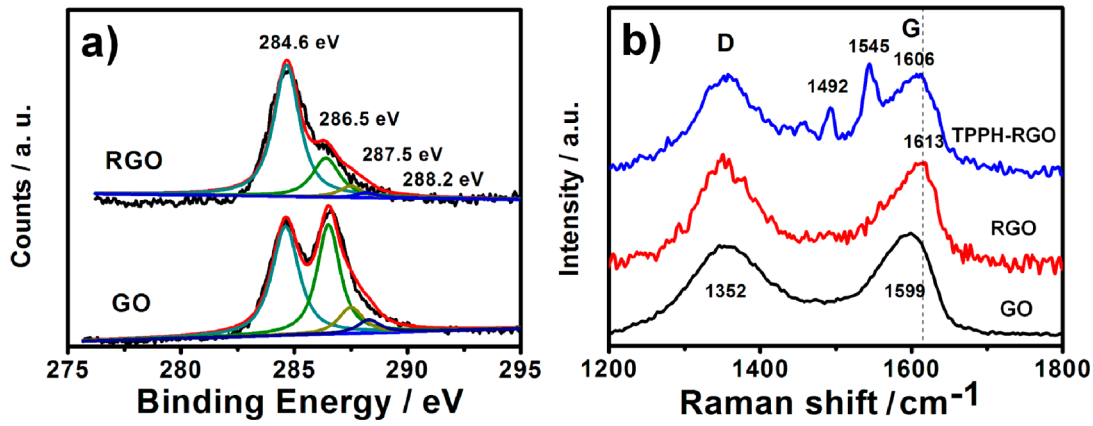

Figure 3. (a) Typical XPS spectra of GO and RGO nanosheets. (b) Raman spectra of GO, RGO, and TPPH–RGO nanospecies.

(Figure 2c) is ca. 1.563 nm, which is higher than RGO species. This could be attributed to the porphyrin molecule adsorption on the surfaces of graphene through $\pi-\pi$ stacking interaction.[49,50] To further test the hybridization of TPPH–RGO nanospecies, the Raman and UV–vis spectra together with XPS spectra of the samples are investigated in the following paragraphs.

To validate successful reduction of the GO sheets, the UV–vis and FT-IR spectra are presented, as shown in Figure S2 and Figure S3 (Supporting Information). The UV–vis spectrum of GO suspension shows a peak centered at 230 nm, which is corresponding to $\pi \rightarrow \pi^*$ transitions of aromatic C=C bonds of GO, while RGO suspension shows an absorption peak centered at 259 nm (Figure S2, Supporting Information).[44,51] The peak shift probably results from the cooperative effect of deoxygenating and part restoration of the electronic conjugation of graphene, which testify the reduction of the GO nanosheets. As shown in Figure S3a and S3b (Supporting Information), the FT-IR spectrum of RGO demonstrates that the intensities of characteristic absorption bands corresponding to the C–O stretching and C=O carbonyl stretching have been significantly reduced compared with the ones of GO, indicating that RGO has less oxygen-containing groups on its surface.[27,43] Those results demonstrated the successful chemical reduction of GO in our experimental process.

XPS is a useful surface chemical analysis technique for determining the element species and chemical states of the surface of materials. To further reveal the deoxygenation of GO during reduction, XPS investigation was conducted, as depicted in Figure 3a. The C 1s peak of the as-prepared GO sheet was deconvoluted into four peaks located at 284.6 (sp^2 carbon, C=C–C bonds), 286.5 (C–O bonds), 287.5 (C=O bonds), and 288.2 eV (O–C=O bonds), respectively, which are consistent with the reported results.[27,29,51] Upon reduction of GO, the intensities of peaks corresponding to the oxygen-containing groups are significantly reduced, while the intensity of the peak corresponding to the C–C at 284.6 eV is enhanced, indicating the removal of most oxygen-containing groups, especially C–O species and recovery of the sp^2 C networks.[27,29,51,52]

Raman spectroscopy is a powerful tool to determine the surface microstructure of carbon-based materials. Therefore, we carried out Raman measurements on GO, RGO, and TPPH–RGO nanospecies, as shown in Figure 3b. In the Raman spectra, all the samples display two prominent bands D (~1352 cm^{-1}) and G (1599–1613 cm^{-1}) corresponding to the breathing mode of κ-point phonons of A_{1g} symmetry and E_{2g} phonons of sp^2 C atoms, respectively. The intensity ratio (I_D/I_G) of the D band to G band of GO is about 0.88, while the I_D/I_G of RGO is about 1.05. The increase of I_D/I_G is attributed to the reduction and restoration of the sp^2 network of GO after the reduction process, which suggest successful reduction of GO.[33,41]

In the Raman spectrum of the TPPH–RGO nanocomposite, the new bands at 1492 and 1545 cm^{-1} are assigned to pyrrole ring C_b-C_b (NH) vibration and pyrrolidine ring C_b-C_b (N) vibration in TPPH, respectively.[53] In addition, it can be observed that the peak position for the G band of RGO is at 1613 cm^{-1}. The peak position of TPPH–RGO is ca. a 6 cm^{-1} shift to a lower frequency compared with RGO. Generally, the G band of RGO in the Raman spectrum is known to be shifted to lower frequencies (softening) when hybridized with an electron-donor component or to higher frequencies (stiffening) when hybridized with an electron-acceptor component.[42,51,54] This ca. 6 cm^{-1} shift to a lower frequency in our TPPH–RGO hybrid compared with the RGO sheet confirms the occurrence of charge transfer between TPPH and RGO in RGO-based hybrid nanocomposites, where TPPH and RGO species work as an electron-donor and electron-acceptor component, respectively.[42,51,54] To further confirm the efficient charge transfer between the TPPH molecule and RGO nanospecies, the optical and photoelectrical properties of the samples are investigated in the following section.

3.2. Optical Properties and Photoelectrical Response Studies. The absorption spectra of RGO and the TPPH–RGO nanocomposite in various compositions are shown in Figure 4. The UV–vis spectrum of RGO shows a broad absorption in the whole measured spectral region and an absorption band centered at 259 nm, which is attributed to the $\pi-\pi^*$ transition of graphene. The UV–vis spectrum of TPPH demonstrates a Soret band, which appears at ca. 420 nm arising from the $a_{1u}(\pi)$ to $e_g^*(\pi)$ transition, and four lower intensity absorption peaks, which are attributed to the Q-bands of $a_{2u}(\pi)$ to $e_g^*(\pi)$ transition. These spectra are consistent with reported results of earlier studies.[14,15] The UV–vis spectrum of TPPH–RGO shows typical absorptions of both moieties of the nanocomposite. However, the band centered at 448 nm attributed to the Soret band of TPPH adsorbed on the RGO nanosheets is found to red shift ca. 28 nm compared with the one of free TPPH. The fact demonstrates $\pi-\pi$ stacking interactions between the individual components in the TPPH–RGO nanocomposite.[49−51] When TPPH concentration in the nanocomposite increases to 5.3×10^{-3} mg mL^{-1}, both light

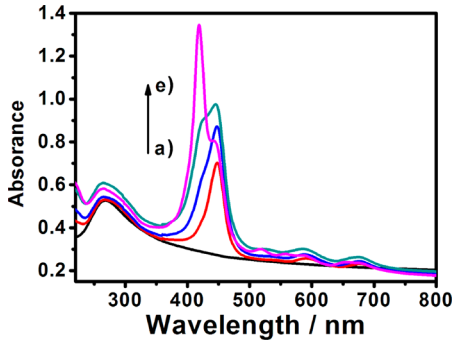

Figure 4. Absorption spectra recorded during the process of adding various volumes of TPPH (0.025 mg mL^{-1}) to 3 mL of RGO aqueous solution (0.03 mg mL^{-1}): (a) 0, (b) 200 μL, (c) 400 μL, (d) 600 μL, and (e) 800 μL.

absorptions of free TPPH and the porphyrin adsorbed on RGO sheets can be observed. This may be due to that there is an adsorption−desorption equilibrium between TPPH and RGO sheets in the solution of the nanocomposite. Thus, the maximum amount of TPPH adsorbed on the RGO sheets is ca. 0.11 mg mg^{-1} in our system.

To investigate the energy/electron transformation between TPPH and RGO nanosheets, the fluorescence spectra of the samples at 420 nm excitation are demonstrated in Figure 5. The

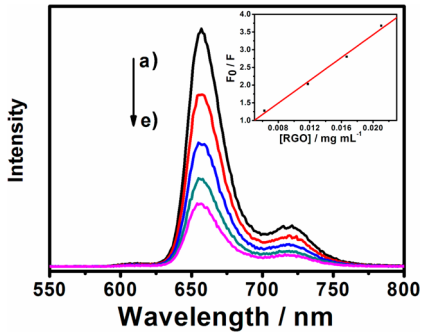

Figure 5. Fluorescence emission spectra recorded during the process of adding various volumes of RGO dispersion (0.1 mg mL^{-1}) to 3 mL of TPPH ethanol solution (0.0125 mg mL^{-1}) at room temperature. (a) 0, (b) 200 μL, (c) 400 μL, (d) 600 μL, and (e) 800 μL. λ_{ex} = 420 nm. The inset is the Stern−Volmer plot of F_0/F vs [Q] for TPPH quenching by RGO sheets.

TPPH solution exhibited a strong fluorescence emission at 657 nm and a shoulder at 720 nm. The fluorescence emission intensity decreased gradually as the content of RGO in the nanocomposite increased. When the content of RGO is about 0.021 mg mL^{-1} in the nanocomposite, the calculated quenching efficiency is 74%. The fluorescence quenching in the TPPH−RGO composites indicates electron transfer from TPPH to RGO, suggesting that RGO is a nice electron acceptor.[13−16,50,54]

The quenching constant of fluorescence K_Q is ca. 161 mL mg^{-1} obtained from the Stern−Volmer formula[55,56]

$$F_0/F = 1 + K_Q[Q] \quad (3)$$

where Q represents the quencher (RGO sheets); F_0 and F are the fluorescence intensities of TPPH in the absence and presence of the RGO sheets. This equation demonstrates a linear relationship between the emission ratio F_0/F and the concentration of the quencher [Q] (Figure 5, inset). Accordingly, it has been further revealed that RGO nanosheets could accept excited electrons of sensitizers in TPPH−RGO nanocomposites under photoexcitation.

To use TPPH−RGO as a photocatalyst for photocurrent generation and hydrogen evolution, we deposited Pt nanoparticles as cocatalyst on the RGO nanosheets and then hybridized with TPPH. The FT-IR spectrum of TPPH−RGO (Figure S3d, Supporting Information) combines RGO and TPPH characteristic absorptions. The peak of C═O stretching vibration of TPPH−RGO occurred at ca. 1735 cm^{-1}, while the C═O stretching vibration of TPPH−RGO/Pt was at 1720 cm^{-1} (Figure S3e, Supporting Information). This ca. 15 cm^{-1} to low wavenumber shift provides evidence of interactions between the Pt nanoparticle and residual carboxyl group on the RGO nanosheet.[13] Figure S4 (Supporting Information) shows the typical TEM image of TPPH−RGO, RGO/Pt, TPPH/Pt, and TPPH−RGO/Pt nanocomposites. From the TEM image of TPPH−RGO (Figure S4a, Supporting Information), the transparent and crimped graphene sheets can be observed. The size of Pt nanoparticles in the TPPH/Pt and RGO/Pt composite is 5.3 ± 0.3 nm and 4.9 ± 0.6 nm, respectively, which is similar to the size of Pt in TPPH−RGO/Pt (5.5 ± 0.5 nm). The XRD pattern of TPPH−RGO/Pt could also demonstrate the Pt nanoparticles generation. As shown in Figure S5 (Supporting Information), the peaks at 39.7, 46.1, and 67.6° correspond to the (111), (200), and (220) crystalline planes of face-centered cubic Pt, respectively.[13−16]

Figure 6 shows the photoelectrical responses of the indium tin oxide (ITO) electrode coated with RGO/Pt, TPPH/Pt, and

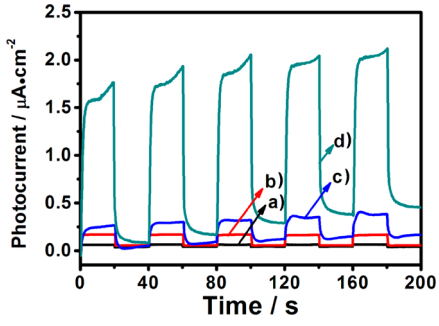

Figure 6. Photocurrent responses of sample (a) ITO, (b) ITO/TPPH/Pt, (c) ITO/RGO/Pt, and (d) ITO/TPPH−RGO/Pt to UV−vis irradiation in 50 mL of TEA aqueous (10 vol %) containing 0.1 M Na_2SO_4 recorded at 0.5 V. The illumination from a 150 W xenon lamp was interrupted every 20 s.

TPPH−RGO/Pt film, respectively. The photocurrent response for the ITO electrode was negligible. Both the ITO/RGO/Pt and ITO/TPPH/Pt electrodes demonstrated prompt photocurrent responses under UV−vis light illumination. However, the photocurrents were relatively weak. An obvious enhanced photocurrent response (1.2 μA cm^{-2}) for the electrode covered with TPPH−RGO/Pt film was observed under similar experimental conditions. The photocurrent response for the TPPH−RGO/Pt film was prompt, steady, and reproducible during repeated on/off cycles of the UV−vis light illumination. The enhancement of the photocurrent for the ITO/TPPH−RGO/Pt electrode compared with ITO/RGO/Pt and ITO/TPPH/Pt electrode is owing to (i) the nice absorption of the TPPH−RGO nanocomposite and (ii) the efficient electron transfer from the photoexcited TPPH moiety to RGO, then to

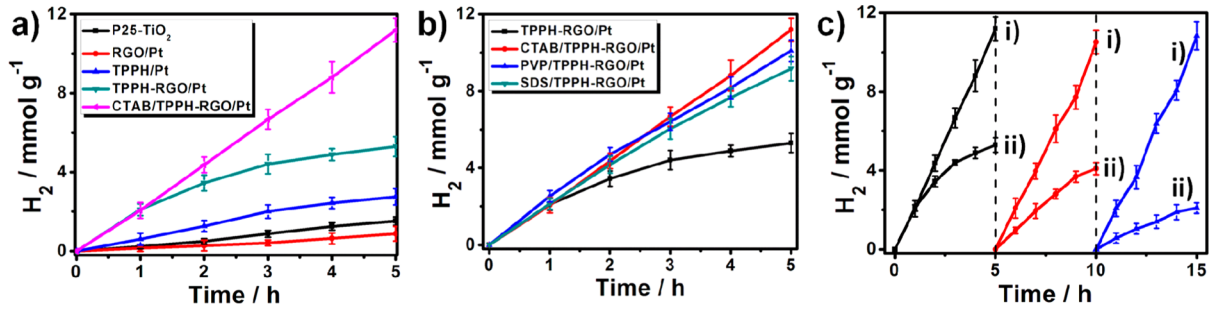

Figure 7. (a) Amount of H_2 evolved from as-prepared photocatalysts using TEA as a sacrificial agent under UV–vis light irradiation. (b) The influence of the surfactants (CTAB, PVP, and SDS) on the amount of H_2 evolved from TPPH–RGO/Pt photocatalyst under UV–vis light irradiation. (c) Re-running of TPPH–RGO/Pt in the presence (i) and absence (ii) of CTAB for hydrogen generation. The reaction was continued for 15 h, with intermittent interruption every 5 h. Reaction conditions: $m_{catalyst}$ = 1 mg, RGO:TPPH = 2:1, [Pt] = 5 wt %, pH = 9, [TEA] = 10 vol %, [surfactant] = 2 mg, T = 298 K.

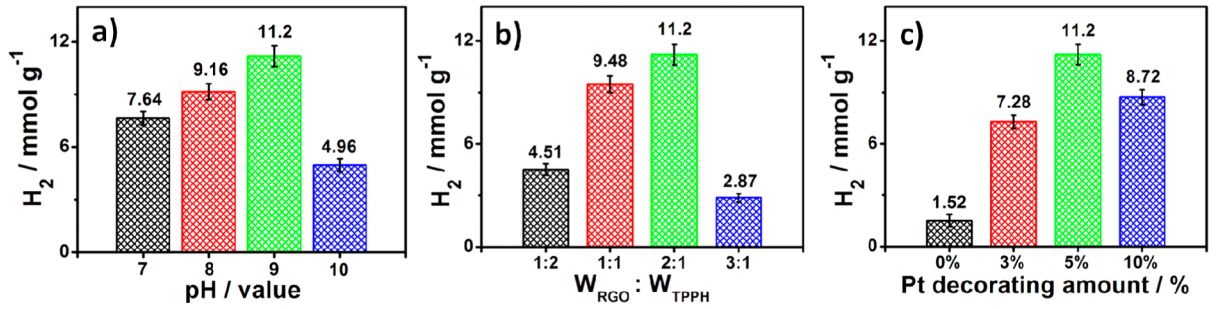

Figure 8. (a) Influence of pH on the amount of H_2 evolved using TPPH–RGO/Pt as the photocatalyst. (b) Effect of the composition of the TPPH–RGO/Pt catalyst on photocatalytic activity for hydrogen production. (c) Dependence of photocatalytic activity of the TPPH–RGO/Pt catalyst on the amount of Pt loaded. Reaction conditions: $m_{catalyst}$ = 1 mg, [TEA] = 10 vol %, [CTAB] = 2 mg, irradiation time = 5 h, T = 298 K.

Pt nanoparticles. Accordingly, the efficient charge separation, which is of benefit to the enhancement of photocurrent in the TPPH–RGO nanocomposite, will certainly be expected to improve photocatalytic activities of the nanocomposite.

3.3. Photocatalytic Hydrogen Evolution. The photocatalytic performances for hydrogen production over P25–TiO_2, RGO/Pt, TPPH/Pt, and TPPH–RGO/Pt in the absence and presence of CTAB under UV–vis light irradiation are shown in Figure 7a. The total amount of H_2 evolved under 5 h UV–vis light irradiation from the system by using P25–TiO_2, RGO/Pt, and TPPH/Pt as photocatalyst are 1.52, 0.89, and 2.74 mmol g^{-1}, respectively, which are distinctly lower than that from the system via using TPPH–RGO/Pt composite as the photocatalyst (5.29 mmol g^{-1}, the apparent quantum yield calculated according to eq 2 is 1.7%). The evident enhancement of the H_2 production from TPPH–RGO/Pt could be attributed to the efficient electron transfer from photoexcited TPPH to Pt nanoparticles through RGO sheets. Herein, RGO acts as a solid-state electron mediator, facilitating charge separation and suppressing recombination of photoexcited electron–hole pairs in the TPPH–RGO nanocomposite.[26]

However, as shown in Figure 7a, the amount of H_2 evolved from the TPPH–RGO/Pt system was maintained at the first 2 h of irradiation, and then it decreased gradually. Interestingly, after adding CTAB in the photocatalytic system, the photocatalytic performance is enhanced distinctly. The amount of H_2 evolved under 5 h UV–vis light irradiation is 11.2 mmol g^{-1}, and the apparent quantum yield calculated according to eq 2 is 3.6%. Furthermore, a continuous and stable H_2 evolution is detected from the system containing CTAB. The enhancement of CTAB to photocatalytic performance might be attributed to an aggregation prevention of TPPH–RGO/Pt during the catalytic process.[46] We also carried out photocatalytic hydrogen evolution of the RGO–TPPH/Pt nanocomposite under visible light (λ > 400 nm) irradiation. As shown in Figure S6 (Supporting Information), hydrogen evolution (0.69 mmol g^{-1}) can be detected from the RGO–TPPH/Pt nanocomposite under 5 h visible light irradiation. This result suggests that the RGO–TPPH/Pt nanocomposite could be used as visible–-light driven photocatalysts.

Figure S7 (Supporting Information) shows photographs of the TPPH–RGO/Pt system in the presence and absence of CTAB surfactant before and after 2 h photoreaction at room temperature. It can be seen that much of TPPH–RGO/Pt nanocomposite adsorbed on the wall of the reaction vessel and the solution was almost transparent after 2 h photoreaction when CTAB surfactant was not added in the system (Figure S7b, Supporting Information). However, when CTAB surfactant was added into the system under ultrasonic treatment, a homogeneous solution was observed after 2 h photoreaction, which suggested that the TPPH–RGO/Pt nanocomposite was well dispersed (Figure S7d, Supporting Information). Owing to electrostatic attraction between positively charged CTAB and negatively charged RGO, CTAB cations could spontaneously assemble on the surface of RGO, which can prevent RGO sheets from aggregation, resulting in a stable system. We also tested the assistance of nonionic surfactant (polyvinyl pyrrolidone, PVP) and anionic surfactant (sodium dodecyl sulfate, SDS) to the photocatalytic reactions. As shown in Figure 7b, these surfactants could also enhance catalytic activity compared with the system without adding surfactant. However, CTAB surfactant in the control

dx.doi.org/10.1021/am302912v | ACS Appl. Mater. Interfaces 2013, 5, 1732–1740

Scheme 1. Schematic Photoexcited Electron Transfer and Hydrogen Evolution Over the RGO−TPPH Photocatalyst with the Assistance of the CTAB under Light Irradiation

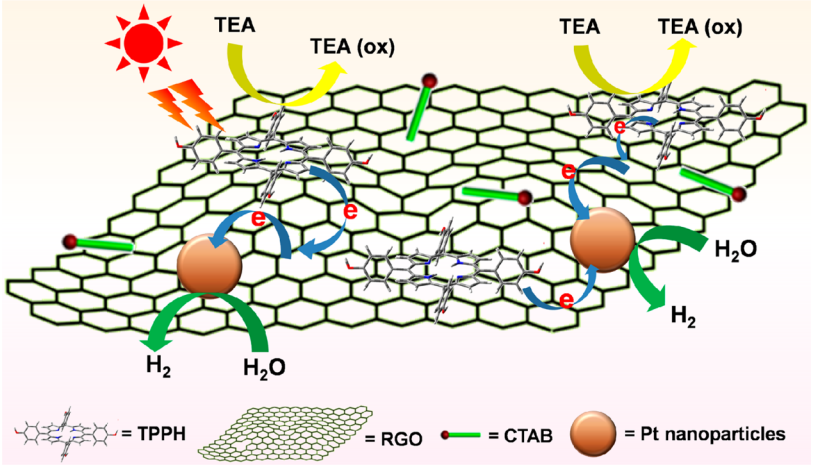

experiments (P25−TiO_2 and TPPH/Pt) did not evidently enhance the photocatalytic activity other than RGO/Pt, as shown in Figure S8 (Supporting Information), since there is no aggregation problem in these photocatalytic reactions. This result suggests that the surfactant can efficiently prevent aggregation of the graphene-based photocatalysts during the photoreaction process.

Due to the importance of the stability of a photocatalyst for its practical application, the photocatalytic stabilization of TPPH−RGO/Pt was tested by cycle photocatalytic hydrogen evolution experiments. The photocatalytic results of the TPPH−RGO/Pt system at the optimum experimental conditions in the presence and absence of CTAB under prolonged irradiation are shown in Figure 7c. The H_2 evolution stopped when the light was switched off. The catalytic system was kept in the dark overnight, and then light irradiation was restarted. The continuous H_2 evolution with no noticeable degradation from the TPPH−RGO/Pt system in the presence of CTAB was observed in the subsequent runs. However, the catalytic activity was decreased noticeabley for the system in the absence of CTAB. This result further indicates that the photocatalytic activity of TPPH−RGO/Pt could be kept stable under the assistance of CTAB.

The dependence of hydrogen production amount on pH of the system using TPPH−RGO/Pt as catalyst is shown in Figure 8a. The pH value of the system influences the hydrogen evolution amount dramatically. When pH value varies from 7 to 10, the maximum average rate of hydrogen evolution is achieved at a pH of 9. The rate of hydrogen evolution decreases as pH value of the system is adjusted to either lower or higher than 9. Both the reduction potential of water and the ability of the donating electron of TEA influence the hydrogen evolution rate. As the pH value decreases, the reduction potential of water augments, raising the hydrogen evolution rate. However, the ability of the donating electron of protonated TEA decreases at low pH, reducing the rate of hydrogen evolution. As the pH value increases, the situation reverses. Thus, photoinduced hydrogen evolution should occur at an optimized pH.

Figure 8b is the influence of the composition of the nanocomposite on the amount of H_2 evolved. The maximum average production amount of H_2 is achieved from the catalytic system using TPPH−RGO (2:1) as the catalyst. As discussed above, there is an adsorption−desorption equilibrium between TPPH and RGO sheets in the solution of the nanocomposite. When the content of TPPH in the TPPH−RGO/Pt nanocomposite is low, the light absorption of the system reduces since the number of TPPH molecules adsorbed on RGO sheets is not enough. Meanwhile, the excess free TPPH molecules in the system may produce a filter effect and cause intermolecular energy transfer, resulting in a decrease of the photocatalytic efficiency.

The photocatalytic activity for H_2 production over the TPPH−RGO/Pt photocatalysts is also optimized by considering the effects of Pt decorating amount. Figure 8c shows the effect of the Pt decorating amount on photocatalytic activity. The amount of H_2 production increases with the increasing Pt decorating amount to a maximum at 5%, while it decreases when the amount of Pt loaded is above 5%. The higher H_2 production over the optimized Pt loading nanocomposite could be attributed to that the Pt nanoparticles can collect the electrons coming from graphene and reduce the forming overpotential of H_2. When Pt loading on the surface of graphene is above the optimum value, some negative effects, such as hindering the interaction between RGO and the TPPH molecule or shielding the photosensitive graphene surface, may occur, consequently diminishing the activity of the catalyst for the photoreaction. Moreover, the TEM images of TPPH−RGO/Pt with various Pt loadings (Figure S9, Supporting Information) show that the size of Pt augments as the Pt loading increases, which would also decrease the catalytic activity.

On the basis of the above results, a possible mechanism for light-driven water reduction to produce H_2 on this graphene-based nanohybrid with the assistance of CTAB can be illustrated in Scheme 1: (1) under UV−vis light irradiation, TPPH molecules adsorbed on RGO sheets are excited, and the photoinduced electrons transfer from the TPPH moiety to RGO; (2) the electrons are then transferred from RGO to Pt nanoparticles loaded on the graphene nanosheets, where the water molecules accept the electrons to form H_2; (3) the photoexcited TPPH moiety returns back to the ground state by accepting electrons from TEA.

4. CONCLUSIONS

In conclusion, we present a simple method to prepare a novel TPPH−RGO/Pt nanocomposite as a photocatalyst for hydro-

gen production from water reduction with the assistance of CTAB. TPPH molecules functionalize RGO via $\pi-\pi$ stacking interactions without much influence on the electronic properties of the RGO. The TPPH moiety in the nanocomposite acts as a photosensitizer and harvesting irradiation light, and the RGO moiety acts as an acceptor and mediator of the electrons. The recombination of photoexcited charges is greatly retarded, and the photocatalytic activity increases. Adding CTAB to the photocatalytic system, the photocatalytic performance and stability are enhanced distinctly compared with one of the systems without CTAB, indicating that surfactant can efficiently prevent the TPPH−RGO nanocomposite aggregation during the photoreaction. This work has demonstrated a CTAB aggregation-prevention assistant TPPH−RGO/Pt system with enhanced catalytic activity and stability, which has potential applications in the fields of light harvesting and photoinduced hydrogen evolution.

■ ASSOCIATED CONTENT

Ⓢ Supporting Information

The photographs and UV−vis sphetra of GO and RGO. FT-IR spectra of GO, RGO, TPPH, TPPH−RGO, and TPPH−RGO/Pt nanocomposites. TEM images of TPPH−RGO, RGO/Pt, TPPH/Pt, and various Pt loading in the TPPH−RGO/Pt. XRD pattern of TPPH−RGO/Pt nanocomposite. The photocatalytic results of the nanocomposite under visible light and control experiments. The photographs of the nanocomposite in the absence and presence of CTAB before and after light irradiation. This material is available free of charge via the Internet at http://pubs.acs.org.

■ AUTHOR INFORMATION

Corresponding Author

*E-mail: pyang@suda.edu.cn. Tel.: (+86)512-65880361. Fax: (+86)512-65880089.

Author Contributions

§These authors contributed equally to this work.

Notes

The authors declare no competing financial interest.

■ ACKNOWLEDGMENTS

The authors are grateful for the financial support of this research by the National Natural Science Foundation of China (21243009, 51273141, and 51073114), the Natural Science Foundation of Jiangsu Province (BK2010209), and the Priority Academic Program Development of Jiangsu Higher Education Institutions (PAPD).

■ REFERENCES

(1) Pimentel, D.; Herz, M.; Glickstein, M.; Zimmerman, M.; Allen, R.; Becker, K.; Evans, J.; Hussain, B.; Sarsfeld, R.; Grosfeld, A.; Seidel, T. *Bioscience* **2002**, *52*, 1111−1120.
(2) Zhang, J.; Wang, Y.; Zhang, J.; Lin, Z.; Huang, F.; Yu, J. *ACS Appl. Mater. Interfaces* **2013**, *5*, 1031−1037.
(3) Thornton, J. M.; Raftery, D. *ACS Appl. Mater. Interfaces* **2012**, *4*, 2426−2431.
(4) Fujishima, A.; Honda, K. *Nature* **1972**, *238*, 37−38.
(5) Osterloh, F. E. *Chem. Mater.* **2007**, *20*, 35−54.
(6) Maeda, K. *J. Photochem. Photobiol. C: Photochem. Rev.* **2011**, *12*, 237−268.
(7) Kudo, A.; Miseki, Y. *Chem. Soc. Rev.* **2009**, *38*, 253−278.
(8) Kitano, M.; Hara, M. *J. Mater. Chem.* **2010**, *20*, 627−641.
(9) Chen, X.; Shen, S.; Guo, L.; Mao, S. S. *Chem. Rev.* **2010**, *110*, 6503−6570.
(10) Dempsey, J. L.; Brunschwig, B. S.; Winkler, J. R.; Gray, H. B. *Acc. Chem. Res.* **2009**, *42*, 1995−2004.
(11) Esswein, A. J.; Nocera, D. G. *Chem. Rev.* **2007**, *107*, 4022−4047.
(12) Wang, M.; Na, Y.; Gorlov, M.; Sun, L. *Dalton Trans.* **2009**, 6458−6467.
(13) Zhu, M.; Li, Z.; Du, Y.; Mou, Z.; Yang, P. *ChemCatChem* **2012**, *4*, 112−117.
(14) Zhu, M.; Han, M.; Du, Y.; Yang, P.; Wang, X. *Dyes Pigm.* **2010**, *86*, 81−86.
(15) Zhu, M.; Lu, Y.; Du, Y.; Li, J.; Wang, X.; Yang, P. *Int. J. Hydrogen Energy* **2011**, *36*, 4298−4304.
(16) Zhu, M.; Dong, Y.; Du, Y.; Mou, Z.; Liu, J.; Yang, P.; Wang, X. *Chem.—Eur. J.* **2012**, *18*, 4367−4374.
(17) Martinez-Diaz, M. V.; de la Torre, G.; Torres, T. *Chem. Commun.* **2010**, *46*, 7090−7108.
(18) Griffith, M. J.; Sunahara, K.; Wagner, P.; Wagner, K.; Wallace, G. G.; Officer, D. L.; Furube, A.; Katoh, R.; Mori, S.; Mozer, A. J. *Chem. Commun.* **2012**, *48*, 4145−4162.
(19) Benniston, A. C. *Phys. Chem. Chem. Phys.* **2007**, *9*, 5739−5747.
(20) Wang, W.-S.; Wang, D.-H.; Qu, W.-G.; Lu, L.-Q.; Xu, A.-W. *J. Phys. Chem. C* **2012**, *116*, 19893−19901.
(21) Peining, Z.; Nair, A. S.; Shengjie, P.; Shengyuan, Y.; Ramakrishna, S. *ACS Appl. Mater. Interfaces* **2012**, *4*, 581−585.
(22) Xiang, Q.; Yu, J.; Jaroniec, M. *Chem. Soc. Rev.* **2012**, *41*, 782−796.
(23) An, X.; Yu, J. C. *RSC Adv.* **2011**, *1*, 1426−1434.
(24) Zhang, N.; Zhang, Y.; Xu, Y.-J. *Nanoscale* **2012**, *4*, 5792−5813.
(25) Yao, Z.; Zhu, M.; Jiang, F.; Du, Y.; Wang, C.; Yang, P. *J. Mater. Chem.* **2012**, *22*, 13707−13713.
(26) Iwase, A.; Ng, Y. H.; Ishiguro, Y.; Kudo, A.; Amal, R. *J. Am. Chem. Soc.* **2011**, *133*, 11054−11057.
(27) Li, Q.; Guo, B.; Yu, J.; Ran, J.; Zhang, B.; Yan, H.; Gong, J. R. *J. Am. Chem. Soc.* **2011**, *133*, 10878−10884.
(28) Xiang, Q.; Yu, J.; Jaroniec, M. *J. Am. Chem. Soc.* **2012**, *134*, 6575−6578.
(29) Xiang, Q.; Yu, J.; Jaroniec, M. *Nanoscale* **2011**, *3*, 3670−3678.
(30) Zhang, J.; Yu, J.; Jaroniec, M.; Gong, J. R. *Nano Lett.* **2012**, *12*, 4584−4589.
(31) Zhang, X.-Y.; Li, H.-P.; Cui, X.-L.; Lin, Y. *J. Mater. Chem.* **2010**, *20*, 2801−2806.
(32) Park, Y.; Kang, S.-H.; Choi, W. *Phys. Chem. Chem. Phys.* **2011**, *13*, 9425−9431.
(33) Li, Y.; Wang, H.; Xie, L.; Liang, Y.; Hong, G.; Dai, H. *J. Am. Chem. Soc.* **2011**, *133*, 7296−7299.
(34) Fan, W.; Lai, Q.; Zhang, Q.; Wang, Y. *J. Phys. Chem. C* **2011**, *115*, 10694−10701.
(35) Ng, Y. H.; Iwase, A.; Kudo, A.; Amal, R. *J. Phys. Chem. Lett.* **2010**, *1*, 2607−2612.
(36) Jia, L.; Wang, D.-H.; Huang, Y.-X.; Xu, A.-W.; Yu, H.-Q. *J. Phys. Chem. C* **2011**, *115*, 11466−11473.
(37) Lv, X.-J.; Fu, W.-F.; Chang, H.-X.; Zhang, H.; Cheng, J.-S.; Zhang, G.-J.; Song, Y.; Hu, C.-Y.; Li, J.-H. *J. Mater. Chem.* **2012**, *22*, 1539−1546.
(38) Mukherji, A.; Seger, B.; Lu, G. Q.; Wang, L. *ACS Nano* **2011**, *5*, 3483−3492.
(39) Min, S.; Lu, G. *Int. J. Hydrogen Energy* **2012**, *37*, 10564−10574.
(40) Mou, Z.; Dong, Y.; Li, S.; Du, Y.; Wang, X.; Yang, P.; Wang, S. *Int. J. Hydrogen Energy* **2011**, *36*, 8885−8893.
(41) Li, Z.; Chen, Y.; Du, Y.; Wang, X.; Yang, P.; Zheng, J. *Int. J. Hydrogen Energy* **2012**, *37*, 4880−4888.
(42) Zhu, M.; Dong, Y.; Xiao, B.; Du, Y.; Yang, P.; Wang, X. *J. Mater. Chem.* **2012**, *22*, 23773−23779.
(43) Min, S.; Lu, G. *J. Phys. Chem. C* **2011**, *115*, 13938−13945.
(44) Kuila, T.; Bose, S.; Mishra, A. K.; Khanra, P.; Kim, N. H.; Lee, J. H. *Prog. Mater. Sci.* **2012**, *57*, 1061−1105.

(45) Georgakilas, V.; Otyepka, M.; Bourlinos, A. B.; Chandra, V.; Kim, N.; Kemp, K. C.; Hobza, P.; Zboril, R.; Kim, K. S. *Chem. Rev.* **2012**, *112*, 6156−6214.
(46) Liang, Y.; Wu, D.; Feng, X.; Müllen, K. *Adv. Mater.* **2009**, *21*, 1679−1683.
(47) Englert, J. M.; Röhrl, J.; Schmidt, C. D.; Graupner, R.; Hundhausen, M.; Hauke, F.; Hirsch, A. *Adv. Mater.* **2009**, *21*, 4265−4269.
(48) Qi, X.; Pu, K.-Y.; Li, H.; Zhou, X.; Wu, S.; Fan, Q.-L.; Liu, B.; Boey, F.; Huang, W.; Zhang, H. *Angew. Chem., Int. Ed.* **2010**, *49*, 9426−9429.
(49) Xu, Y.; Zhao, L.; Bai, H.; Hong, W.; Li, C.; Shi, G. *J. Am. Chem. Soc.* **2009**, *131*, 13490−13497.
(50) Tu, W.; Lei, J.; Zhang, S.; Ju, H. *Chem.—Eur. J.* **2010**, *16*, 10771−10777.
(51) Geng, J.; Jung, H.-T. *J. Phys. Chem. C* **2010**, *114*, 8227−8234.
(52) Wang, D.-H.; Jia, L.; Wu, X.-L.; Lu, L.-Q.; Xu, A.-W. *Nanoscale* **2012**, *4*, 576−584.
(53) Akins, D. L.; Guo, C.; Zhu, H. R. *J. Phys. Chem.* **1993**, *97*, 3974−3977.
(54) Ghosh, A.; Rao, K. V.; George, S. J.; Rao, C. N. R. *Chem.—Eur. J.* **2010**, *16*, 2700−2704.
(55) Zhang, L.; Lu, Y.; Du, Y.; Yang, P.; Wang, X. *J. Porphyrins Phthalocyanines* **2010**, *14*, 540−546.
(56) Huang, T.; Murray, R. W. *Langmuir* **2002**, *18*, 7077−7081.